J. Fluid Mech. (2008), *vol.* 600, *pp.* 245–256.
doi:10.1017/S0022112008000372 Printed in the United Kingdom

Experimental and numerical investigation of inertial particle clustering in isotropic turbulence

JUAN P. L. C. SALAZAR[1], JEREMY DE JONG[2], LUJIE CAO[2], SCOTT H. WOODWARD[2], HUI MENG[2] AND LANCE R. COLLINS[1]†

[1]Sibley School of Mechanical & Aerospace Engineering, Cornell University, Ithaca, NY 14853–7501, USA

[2]Mechanical & Aerospace Engineering, State University of New York at Buffalo, Buffalo, NY 14260–4400, USA

(Received 15 June 2007 and in revised form 20 December 2007)

This paper presents the first detailed comparisons between experiments and direct numerical simulations (DNS) of inertial particle clustering in nearly isotropic 'box turbulence'. The experimental system consists of a box 38 cm in each dimension with fans in the eight corners that sustain nearly isotropic turbulence in the centre of the box. We inject hollow glass spheres with a mean diameter of 6 μm and measure the locations of several hundred particles in a $1\,\mathrm{cm}^3$ volume in the centre of the box using three-dimensional digital holographic particle imaging. We observe particle concentration fluctuations that result from inertial clustering (sometimes called 'preferential concentration'). The radial distribution function (RDF), a statistical measure of clustering, has been calculated from the particle position field. We select this measure because of its relevance to the collision kernel for particles. DNS of the equivalent system, with nearly perfect parameter overlap, have also been performed. We observe good agreement between the RDF predictions of the DNS and the experimental observations, despite some challenges in the interpretation of the experiments. The results provide important guidance on ways to improve the measurement.

1. Introduction

Numerical simulations of inertial particles in turbulence have shown that the particles tend to cluster outside of vortices, in the high-strain regions of the flow (Squires & Eaton 1991; Eaton & Fessler 1994). Maxey (1987) correctly attributed this effect to the centrifugal force acting on the particles in regions of high rotation, and showed that the divergence of the particle velocity is not zero, but is proportional to the local difference between the squares of the rate-of-strain and rate-of-rotation tensors. The effect can give rise to rather dramatic non-uniformity of the particle concentration field. Particle clustering can influence a broad range of aerosol processes, such as particle settling (Wang & Maxey 1993; Aliseda *et al.* 2002), evaporation/condensation (Shaw *et al.* 1998), and interparticle collisions (Wang, Wexler & Zhou 2000). Sundaram & Collins (1997) identified the radial distribution function (RDF), evaluated at contact, as the precise correction to the collision kernel

† Author to whom correspondence should be addressed: LC246@cornell.edu

to account for clustering. The RDF is a measure of the probability of finding a second particle at a given separation distance from a test particle (McQuarrie 1976). The RDF can be computed from a field of M particles by binning the particle pairs according to their separation distance, and calculating

$$g(r_i) = \frac{N_i/\Delta V_i}{N/V}\ , \tag{1.1}$$

where N_i is the number of particle pairs separated by a distance $r_i \pm \Delta r/2$, ΔV_i is the volume of the discrete shell located at r_i, $N = M(M-1)/2$ is the total number of pairs and V is the total volume of the system. The subscript 'i' is the discrete index and does not refer to a vector quantity. Direct numerical simulations (DNS) have shown the RDF can reach values in excess of 100 for certain parameter values (Reade & Collins 2000*a*; Wang *et al.* 2000). Subsequent numerical work has quantified the dependence of the RDF on the particle Stokes number, and, to a lesser extent, the Reynolds number (Collins & Keswani 2004). Theoretical investigations have yielded predictions of the RDF under a variety of assumptions (Falkovich, Fouxon & Stepanov 2002; Zaichik & Alipchenkov 2003; Chun *et al.* 2005). All of the results suggest that inertial clustering could profoundly influence the evolution of the size distribution of a coalescing aerosol.

Particle clustering may play an important role in the development of convective clouds in the atmosphere. Cloud droplets below 20 μm in diameter are known experimentally to have fairly low collection efficiencies; hence, most cloud models assume droplets grow by condensation alone until they reach a critical size. However, these models underpredict the breadth of the droplet size distribution and overpredict the time required for warm rain initiation by as much as one order of magnitude (Shaw 2003). Shaw *et al.* (1998) hypothesized that droplet clustering may induce vapour supersaturation fluctuations that will broaden the droplet size distribution. Falkovich *et al.* (2002) argued that clustering-enhanced collisions may compensate for the lower efficiency of smaller droplets. Additionally, Reade & Collins (2000*b*) observed that particle inertia tends to broaden the size distribution of a coalescing aerosol.

Although the above arguments provide plausible explanations for the acceleration of cloud development in the atmosphere, quantitative measurement of inertial clustering remains largely based on DNS. There have been a few experimental images of clustered particles in turbulence (Eaton & Fessler 1994); however, only recently have those measurements become quantitative. Wood, Hwang & Eaton (2005) measured a two-dimensional projection of the RDF of entrained particles in a turbulence box by shining a laser sheet at the particles, and measuring their x–y locations with a camera. They found clear evidence of clustering, albeit at levels lower than those found in the DNS study by Sundaram & Collins (1999). One possible explanation for the discrepancy is an attenuation effect due to the reduced dimension of the measurement, as described by Holtzer & Collins (2002). Saw *et al.* (2007) measured the one-dimensional RDF by sampling droplet arrivals at a fixed volume in a wind tunnel. Arrival statistics were used to compute the one-dimensional projection of the RDF, which too is susceptible to the error discussed in Holtzer & Collins (2002).

In this paper, we compare heretofore unavailable experimental measurements of the three-dimensional RDF of particles in a 'turbulence box' with DNS under conditions of excellent parametric overlap. These unique measurements were conducted using a cutting-edge digital holographic imaging technique, which provides three-dimensional particle locations. Spatial accuracy of the particle positions is such that the RDF can be calculated reliably up to $r/\eta \sim 1$, where $\eta = (\nu^3/\epsilon)^{1/4}$ is the Kolmogorov length scale,

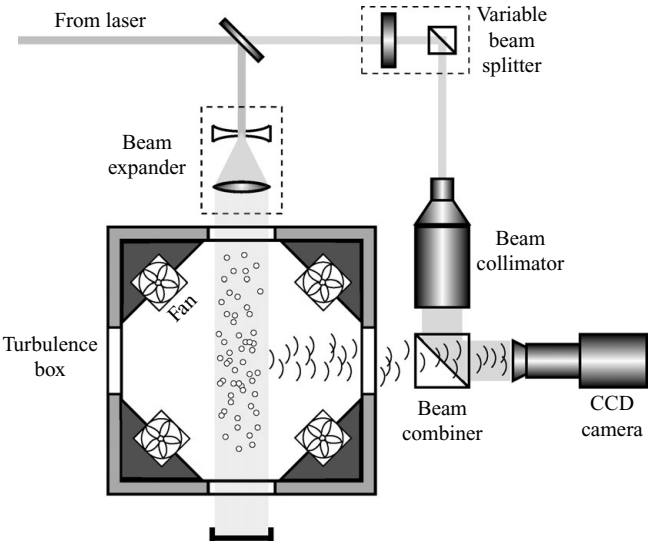

FIGURE 1. Schematic of the turbulence box and holographic imaging set-up.

ν is the fluid kinematic viscosity and ϵ is the turbulent energy dissipation rate. These measurements suffer from none of the effects described above owing to projection of the RDF to lower dimensions. The particle size distribution is moderately broad and, because of resolution limitations, the holographic imaging system may not be able to capture the smaller particles. We input an equivalent distribution of particles into the DNS that closely matches the distribution in the experiment, and then apply a high-pass particle size threshold filter to the DNS results to mimic the filtering done by the digital camera.

2. Experimental method

2.1. *Flow and particle characteristics*

The turbulent flow facility consists of an air chamber ('turbulence box') that is 38 cm across, with fans in the eight corners of the box to produce the turbulent flow field (see figure 1). The design of the box is similar to that used by Birouk *et al.* (1996). The flow field in the central region of the the box has been shown by de Jong *et al.* (2007) to be homogeneous and isotropic. Flow velocity statistics were obtained by particle image velocimetry (PIV), with use of a Spectra-Physics PIV-400 dual injection-seeded Nd:YAG laser (400 mJ pulse^{-1} at 532 nm, 8 ns pulse width) and a sharpVISION 1300 CCD camera (10 bit, 1280×1024, 6.7 μm pixel array). The set-up is able to reach a Reynolds number based on the Taylor microscale, R_λ, up to 187. However, because of concerns with achieving stationary statistics for the RDF that will be discussed later, we have limited the maximum Reynolds number in the experiments to $R_\lambda \sim 150$. A summary of all of the relevant flow parameters for each of the conditions investigated is given in table 1. The turbulent energy dissipation rate ϵ reported in table 1 is calculated via the longitudinal second-order structure function $D_{LL}(r)$, assuming inertial subrange scaling $D_{LL}(r) = C_2(\epsilon r)^{2/3}$ with a universal constant $C_2 = 2.1$ (Sreenivasan 1995). Figure 2 shows two independent measurements of the second-order longitudinal structure function in compensated coordinates, such

	Units	I	II	III
Experiment				
Horizontal r.m.s velocity $u_{\rm rms}$	$\mathrm{m\,s^{-1}}$	0.346 ± 0.005	0.529 ± 0.008	0.672 ± 0.010
Vertical r.m.s velocity $v_{\rm rms}$	$\mathrm{m\,s^{-1}}$	0.378 ± 0.005	0.582 ± 0.008	0.764 ± 0.011
Turbulent kinetic energy k	$\mathrm{m^2\,s^{-2}}$	0.191 ± 0.004	0.449 ± 0.009	0.743 ± 0.016
Turbulent intensity $u' = \sqrt{2/3k}$	$\mathrm{m\,s^{-1}}$	0.357 ± 0.004	0.547 ± 0.006	0.704 ± 0.007
Turbulent energy dissipation rate ϵ	$\mathrm{m^2\,s^{-3}}$	1.33 ± 0.21	4.90 ± 0.76	11.0 ± 1.73
Large eddy length scale $L = k^{3/2}/\epsilon$	cm	6.29 ± 0.99	6.13 ± 0.96	5.82 ± 0.94
Large eddy time scale $T_e = L/u'$	s	0.18 ± 0.028	0.11 ± 0.018	0.08 ± 0.013
Kolmogorov length scale η	μm	226 ± 8.7	163 ± 6.3	133 ± 5.2
Kolmogorov time scale τ_η	10^{-3}s	3.37 ± 0.27	1.76 ± 0.14	1.17 ± 0.09
Kolmogorov velocity scale u_η	$\mathrm{m\,s^{-1}}$	0.067 ± 0.003	0.093 ± 0.004	0.114 ± 0.005
Taylor micro-scale λ	mm	4.66 ± 0.37	3.72 ± 0.29	3.19 ± 0.26
Reynolds number R_λ	—	110 ± 9	135 ± 12	149 ± 13
Direct numerical simulations				
Reynolds number R_λ	—	108	134	147

TABLE 1. Flow parameters. Roman numerals indicate the different comparison conditions. We show 95% confidence intervals that were estimated using the method described by Benedict & Gould (1996) for the turbulence velocity statistics and Kline & McClintock (1953) for ϵ and related quantities. Further details can be found in de Jong *et al.* (2007).

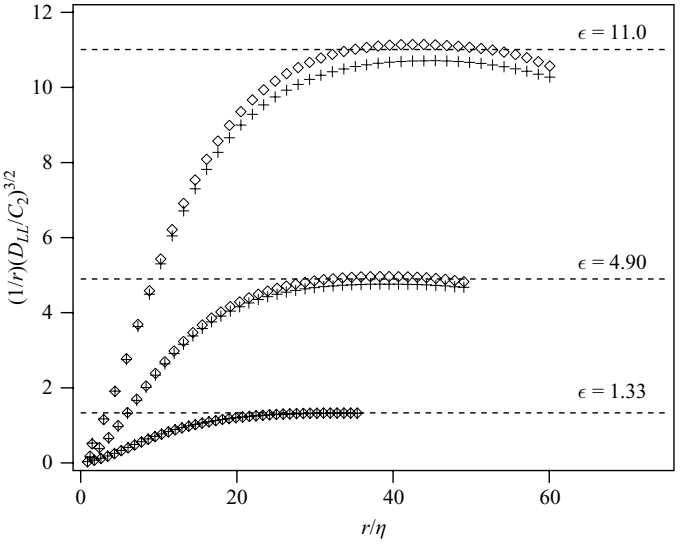

FIGURE 2. Compensated second-order longitudinal structure functions (D_{LL}) for the different flow conditions. Symbols indicate independent realizations of the experiment.

that the ordinate value of the plateau region is ϵ. Refer to de Jong *et al.* (2007) for a complete discussion of the measurement of the dissipation rate in our system.

DNS has shown that the degree of particle clustering is a strong function of the particle Stokes number, defined here as $St \equiv \tau_p/\tau_\eta$, where $\tau_p \equiv \beta d^2/18\nu$ is the viscous response time of the particle, $\tau_\eta \equiv \sqrt{\nu/\epsilon}$ is the Kolmogorov time scale, $\beta \equiv \rho_p/\rho$ is the ratio of the particle density to the fluid density and d is the particle diameter. Maximum clustering occurs for $St \sim 1$. In an attempt to maximize the signal-to-noise ratio in the experiment, we selected silver-coated hollow-glass spheres ($\beta = 1375$). The

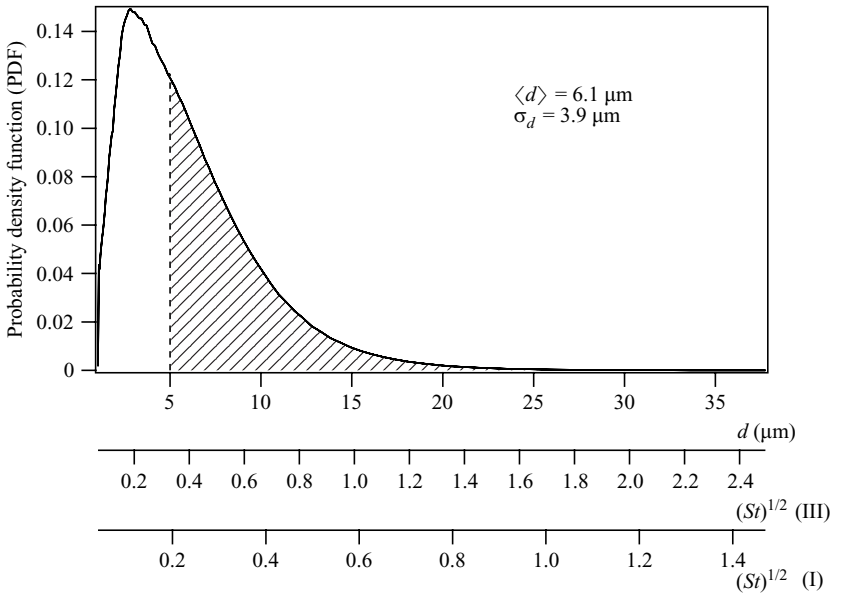

FIGURE 3. Particle size and particle Stokes PDFs for I and III. The particle size PDF was measured by a third party using the electrozone particle sensing technique. A sample filtering operation is shown for $d_c = 5\,\mu$m.

probability density function (PDF) of the particle size is shown in figure 3, both in terms of diameter and the corresponding Stokes number at the lowest and highest turbulence conditions in the study. Clearly, there is a broad range of particle Stokes numbers, peaked between 0.1 and 0.2 depending upon the fan speed. This range of Stokes numbers allows us to observe a good degree of particle clustering in the experiment.

Experiments were initiated by setting the fans to a particular condition and allowing the system to equilibrate. Particles were then injected into the top of the box, while the digital camera simultaneously recorded holograms at $\sim$10 Hz. Gravitational settling, as well as adhesion to box and fan surfaces, led to a decrease in the particle concentration over time; consequently, particles had to be re-injected periodically to sustain the concentration in the experimental volume within the desired range. The negligible particle mass loadings in the experiment ($O(10^{-4})$) led us to believe that the measured turbulence conditions were not substantially altered by particle injection, although we could not simultaneously measure particle and velocity field statistics.

2.2. *Holographic imaging*

Digital holographic imaging, as in digital holographic PIV, employs a digital image sensor to record the hologram, and uses numerical algorithms to reconstruct the three-dimensional image volume (Xu *et al.* 2001; Owen *et al.* 2002; Pan & Meng 2003). It eliminates the notorious wet film processing of individual holograms and enables continuous-in-time three-dimensional volumetric particle/flow measurements. However, the low resolution of digital image sensors has restricted standard digital particle holography to the in-line configuration (forward scattering). The narrow angular spread of the in-line hologram recording, along with the finite digital sensor pixel size causes severe speckle noise and a large depth-of-focus in the reconstructed particle image. Consequently, the current generation of digital holographic imaging

systems is limited to measurements at low particle densities ($<1\,\mathrm{mm}^{-3}$) and small flow facilities (<1 cm in each dimension).

The large size of our particle-laden turbulence chamber and the dense particle distribution prohibit the use of standard digital in-line holography owing to its excessive speckle noise. We therefore employ a hybrid digital holographic system described in Meng, Pan & Pu (2004) and Cao *et al.* (2007). In this approach (figure 1), the pulsed laser beam is split into a reference beam and an object illumination beam, allowing a selected volume of particles in the turbulence box to be imaged at 90°. The selected illumination and arrangement of 90° scattering avoids the excessive speckle noise from particles along the illumination path that are outside the volume of interest, as would occur in standard digital in-line holography. The 90° scattered light is then recorded via interference with the reference beam, which is folded into the hologram's optical axis. The recombination of the object and reference beams on-axis minimizes the spatial frequency of the holographic fringes, such that these can be resolved by the digital sensor. Such a design has the advantages of speckle-noise suppression provided by off-axis (side) scattering and the lower resolution requirement provided by on-axis (in-line) recording. Hence, the hybrid system enables three-dimensional measurements in large flow facilities with significant particle concentrations. At this point, we are unable to quantify systematic errors that may result from speckle noise, but we believe them to be small.

One challenge of the hybrid system is that side scattering does not allow the use of the complex amplitude method described in Pan & Meng (2003), designed to reduce the depth-of-focus and improve spatial resolution. Fortunately, images formed by 90° scattering inherently have up to an order of magnitude higher intensity-based axial definition than those formed by forward scattering; thus we employ an intensity-based method to extract particle centroids from the reconstructed hologram, as described in Pan (2003). However, as intensity-based methods rely on thresholding of the reconstructed intensity field, smaller particles in a polydisperse distribution that have lower scattering intensity inevitably are lost during the thresholding, resulting in a particle size 'high-pass' filtering effect. Therefore, to achieve an accurate comparison between our experiments with a polydisperse distribution and DNS, this filtering effect must be taken into account.

Even with the hybrid scheme set for a relatively modest measurement volume of approximately $1\,\mathrm{cm}^3$, the extracted particle density ($\sim 2\,\mathrm{mm}^{-3}$) and number of particles extracted per hologram ($\sim$400) are both well below DNS values. To obtain acceptable statistical convergence, we must average over multiple holograms, weighted by the number of particles in each hologram.

3. Direct numerical simulations

The simulation domain consists of a three-dimensional cube of length 2π along each side (arbitrary units). Periodic boundary conditions make the flow-field amenable to Fourier spectral methods.

3.1. *Governing equations*

The fluid is governed by the continuity and incompressible Navier–Stokes equations

$$\nabla \cdot \boldsymbol{u} = 0\ , \quad \frac{\partial \boldsymbol{u}}{\partial t} + \boldsymbol{u} \cdot \nabla \boldsymbol{u} = -\frac{1}{\rho}\nabla p + \nu \nabla^2 \boldsymbol{u} + \boldsymbol{F}, \tag{3.1}$$

where $\boldsymbol{u}(\boldsymbol{x}, t)$ is the fluid velocity $p(\boldsymbol{x}, t)$ is pressure and $\boldsymbol{F}(\boldsymbol{x}, t)$ is a time-dependent deterministic forcing function that injects energy into the first two wavenumbers to maintain statistically stationary isotropic turbulence (Witkowska, Brasseur & Juvé 1997). The influence of the particle volume on the continuity equation has been neglected owing to the low particle volume loadings, $\Phi_v \sim O(10^{-7})$. Note the absence of a particle source term in the momentum equation. Reverse coupling is neglected, a simplification which is justified owing to the neglibile mass loadings, $\Phi_m \sim O(10^{-4})$ (Boivin, Simonin & Squires 1998; Sundaram & Collins 1999). Particles in the flow field are advanced according to the evolution equation derived by Maxey & Riley (1983), which for large particle-to-fluid density ratios (i.e. $\beta \gg 1$) simplifies to

$$\frac{\mathrm{d}\boldsymbol{x}_p^{(i)}}{\mathrm{d}t} = \boldsymbol{v}_p^{(i)}\ , \quad \frac{\mathrm{d}\boldsymbol{v}_p^{(i)}}{\mathrm{d}t} = \frac{\boldsymbol{u}\left[\boldsymbol{x}_p^{(i)}\right] - \boldsymbol{v}_p^{(i)}}{\tau_p^{(i)}}, \tag{3.2}$$

where $\boldsymbol{v}_p^{(i)}$ is the velocity of the ith particle and $\boldsymbol{u}[\boldsymbol{x}_p^{(i)}]$ is the fluid velocity interpolated at the particle position $\boldsymbol{x}_p^{(i)}$. Additionally, we neglect gravitational settling. Wang & Maxey (1993) found no appreciable effect of gravitational settling on the particle concentration statistics for $v_g/u_\eta < 3$, where $v_g = \tau_p g$ is the gravitational settling velocity and $u_\eta = (\nu\epsilon)^{1/4}$ is the Kolmogorov velocity scale. In our simulations, $v_g/u_\eta \leqslant 1$ for all of the particles at all flow conditions. Moreover, 71%, 82% and 89% of the particles after filtering (see § 3.3) have a settling velocity that is less than 10% of the Kolmogorov velocity scale in flow conditions I, II and III, respectively. Interparticle collisions are also neglected (Reade & Collins 2000*a*).

3.2. *Numerical details*

Equations (3.1) are solved on a 256^3 grid using a pseudospectral method. Details of the numerical method can be found in Brucker *et al.* (2007).

We initialize 600 128 particles with a Stokes (and response time) PDF that matches the experimental PDF shown in figure 3. Heun's method (two-stage second-order Runge–Kutta) is used to numerically integrate (3.2) along each independent particle trajectory with use of an integrating factor. Fluid velocities at particle centres are obtained via an eighth-order Lagrangian interpolation scheme similar to that described in Berrut & Trefethen (2004). Particle response times for the smallest particles are much smaller than the smallest fluid mechanical time scale, τ_η. Reducing the overall time step to update these particles accurately would be extremely wasteful of the CPU. Instead, the particle updates are 'sub-cycled,' wherein multiple particle time steps are taken per fluid time step, resulting in a more accurate description of the particle motions with only a modest increase in CPU.

3.3. *Filtering*

The finite resolution of the camera used to record the digital holograms restricts the range of particle sizes that can be accurately recorded. The camera pixel size is approximately 6.5 μm, hence we expect the camera will filter particles of that size or smaller. Unfortunately, we have no *a priori* means of knowing which particles will be filtered. To mimic the finite resolution of the camera, we apply a high-pass particle size threshold filter with a variable diameter cutoff, d_c. Figure 3 shows the high-pass filter for a cutoff diameter, $d_c = 5\,\mu\mathrm{m}$. Particles in the hatched region are used to compute the RDF. By varying the filter cutoff diameter over a reasonable range, $0\,\mu\mathrm{m} \leqslant d_c \leqslant 10\,\mu\mathrm{m}$, we observe the sensitivity of the RDF (see the inset in figure 5). Our approach is to fit d_c at one fan speed, and test the agreement between DNS and

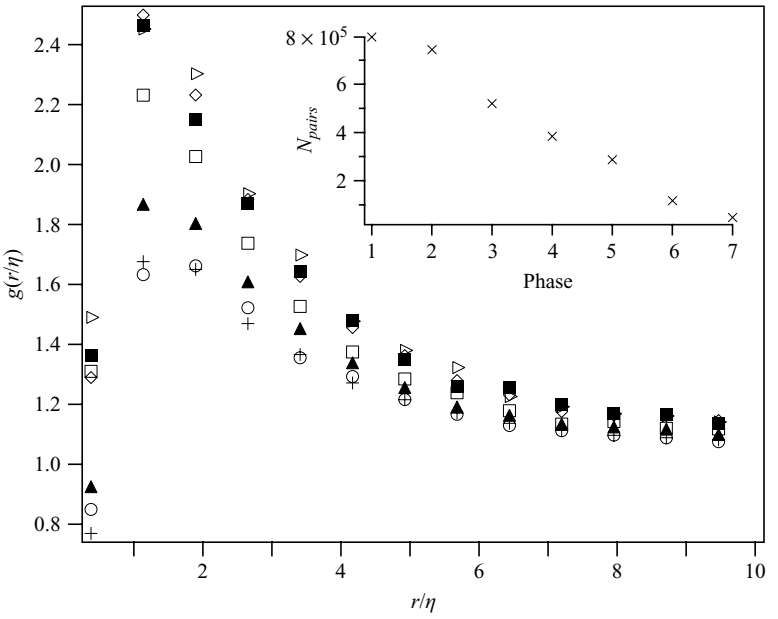

FIGURE 4. A time series of RDFs (III) and number of particle pairs in each phase (inset): +, phase 1; ○, phase 2; ▲, phase 3; □, phase 4; ◇, phase 5; ■, phase 6; ▷, phase 7.

experiments at the other fan speeds, under the assumption that d_c is not sensitive to the conditions of the experiment.

4. Results and discussion

At the conditions summarized in table 1, the RDF was computed by binning the particle pairs based on their separation distance, according to (1.1). The experimental volume is not periodic, thus making the analysis of particles near the boundaries ambiguous. To eliminate any bias from these particles, we treated the volume as periodic and paired those particles with reflected particles from elsewhere in the volume. Numerical experiments with DNS data (taken over non-periodic subdomains) showed the error associated with this assumption to be small.

One unanticipated feature we observed is that following injection, the RDF evolves towards a stationary state. This can be seen in figure 4, which shows the RDF averaged over seven 'phases' following an injection. As shown in the inset of figure 4, the particle concentration is decreasing in time owing to settling and losses to the fan and wall surfaces. When the particle number dropped below the detectable limit, we injected additional particles, causing the transient process to restart. Each 'phase' corresponds roughly to 0.5 s following the peak in the particle concentration of the injection cycle. The steady increase in the RDF over phases 1–5 is at least qualitatively similar to the build-up in the RDF observed in DNS at short times, starting from an initially random particle field. However, precise timings of the injection events were not made in this study, as we had not anticipated the transient behaviour that was observed. Thus, the focus of this study will be on the stationary behaviour we measured in the final two phases.

DNS at flow conditions that match the R_λ from each of the three experimental conditions were performed. Particles with an identical Stokes number distribution

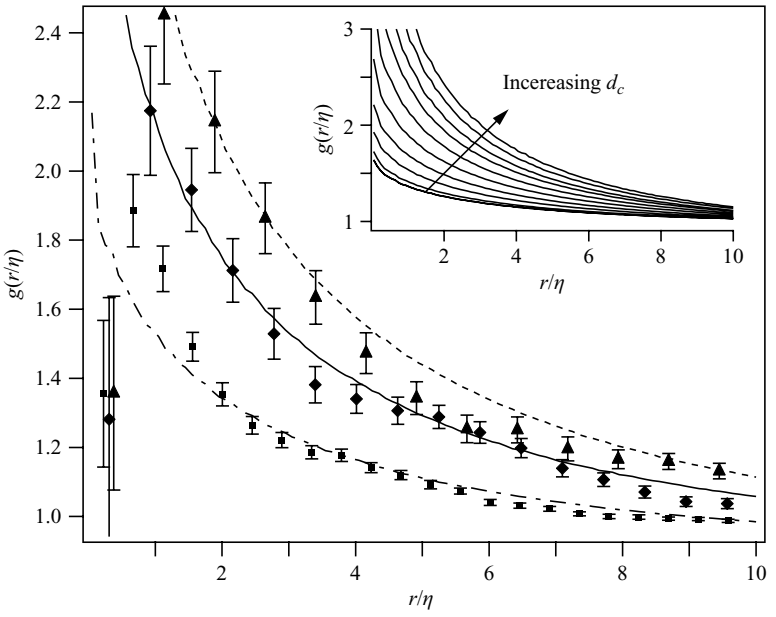

FIGURE 5. RDFs from experiment and DNS ($d_c = 8\,\mu$m). Error bars give the 95% confidence interval obtained via bootstrap: —— – ——, I (DNS); ——, II (DNS); – – –, III (DNS); ■, I (Exp.); ◆, II (Exp.) ; ▲, III (Exp.). Inset shows DNS RDFs (III) for $d_c = 0, 1, \ldots, 10$ μm. For $d_c = 8$ μm: $\langle St \rangle = 0.21$ (I); $\langle St \rangle = 0.40$ (II); $\langle St \rangle = 0.60$ (III).

for each experiment were introduced randomly, and the simulations were run for 10 τ_{eddy}, where $\tau_{eddy} \equiv L_{11}/u'$ is the large eddy turnover time, L_{11} is the longitudinal integral length scale and u' is the turbulence intensity. The DNS was continued for an additional 23 τ_{eddy} and the RDF was computed every 0.2 τ_{eddy} and averaged over the stationary period. The resulting statistical convergence of the RDF was substantially higher than in the experiments.

A complication in comparing the RDF from the experiments and DNS is that even for identically distributed particles, the RDF is sensitive to the size of the experimental volume. This can be understood by recognizing that the RDF (see (1.1)) is normalized by the average pair density in the experimental volume V. Because of clustering, the average pair density for a small sample volume (such as that found in our experiments) will be larger than the corresponding value in the thermodynamic limit $V \to \infty$. To compensate, we renormalized the DNS RDF such that the average pair density used was based on the equivalent sample volume as in the experiment, measured in Kolmogorov units.

The RDFs for conditions I, II and III of table 1 are displayed in figure 5. As discussed in §3.3, the limited resolution of the camera filters the smaller particles. We compensate for the camera's filtering by introducing a high-pass particle-size threshold filter with a cutoff d_c. As shown in the inset of figure 5, the RDF increases with increasing d_c. Because the particles removed by the filtering process have smaller Stokes numbers, their presence lowers the RDF, or conversely their removal increases it. The high-pass filter of $d_c = 8$ μm applied to DNS data shows the best agreement with the experiments at all three conditions. Note that we neglect the first experimental point that is low owing to spatial measurement errors (particularly in the axial direction) and statistical sampling errors. Aside from that point, the remainder of the

	D_2		c_1		$\tilde{c}_1$	
	Exp.	DNS	Exp.	DNS	Exp.	DNS
Case I	2.72	2.79	0.25	0.20	0.28	0.21
Case II	2.56	2.67	0.34	0.32	0.44	0.33
Case III	2.51	2.59	0.40	0.39	0.49	0.41

TABLE 2. Correlation dimension, D_2, and the power-law exponent, c_1, from direct numerical simulations (DNS) and experiments (Exp.) at the three conditions. Also shown is the expression $\tilde{c}_1 = d - D_2$ for $d = 3$.

experimental points are generally in quantitative agreement with the DNS. There are some discrepancies at $r/\eta \sim 5$, mainly due to a bump in the experimental points that we do not observe in the DNS, and for which we have no satisfactory explanation. A second discrepancy occurs at the lowest fan speed for $r/\eta \leqslant 2$. We could match these points by setting $d_c = 9$; however, we cannot justify this change.

An alternative measure of inertial particle clustering is the correlation dimension, D_2 (Grassberger & Procaccia 1983). Bec *et al.* (2007) used this measure to quantify particle clustering. Table 2 shows the good agreement between D_2 obtained by non-linear regression of the experimental measurements and D_2 from the DNS with filter $d_c = 8$ μm. Chun *et al.* (2005) predicted the RDF for monodisperse particles should behave as a power law of the form $g(r) \sim (\eta/r)^{c_1}$. For a power-law RDF, the power c_1 is related to the correlation dimension as follows: $c_1 = d - D_2$, where $d = 3$ is the dimension of the space containing the particles. Table 2 shows a comparison of the values of c_1 obtained by regression of both data sets, and we see once again there is good agreement between experiment and simulations. The expected relationship between c_1 and D_2 ($\tilde{c}_1$ in table 2) is better satisfied by the DNS than by the experimental data. This is mainly attributed to the lower statistical error in the DNS relative to the experiment.

The filtering operation we implemented in the DNS analysis is a crude approximation of the complex filtering performed by the camera. We anticipate the camera will give rise to a convolution of the size distribution rather than a strict high-pass filter. That is, the resolution of a particle of a given size will depend upon the number and size of the neighbouring particles that surround it. We have explored this more complex filtering process by generating synthetic digital holograms using DNS particle positions. We ultimately selected the high-pass filter for its simplicity. We could not justify introducing a more complex function at this time, particularly given the other uncertainties in the experiment, and the difficulty of precisely matching the experiment in the DNS. Our results support our contention that the high-pass filter is able to capture the primary effect of the filtering by the CCD camera.

5. Conclusions

Three-dimensional measurements of the positions of a polydisperse distribution of inertial particles in homogenous and isotropic box turbulence were performed using digital holography. Radial distribution functions were calculated from measurements at three flow conditions. For the first time, quantitative comparisons of the experimentally obtained RDF were made with results from direct numerical simulations performed on a 256^3 grid with 600 128 particles. Near perfect parameter overlap was achieved in terms of the particle Stokes number PDF and flow Reynolds

number. A simple high-pass particle size threshold filter was introduced in the numerical results to mimic the resolution limitations of the CCD camera. We find very good agreement between experiment and DNS based on a filter cutoff $d_c = 8\,\mu\text{m}$. This value is reasonable, given the camera pixel size is $6.7\,\mu\text{m}$.

In future experiments, we plan to address the filtering problem by using a narrower particle size distribution. In addition, work is underway to extend the analysis of Pan & Meng (2003) to the hybrid scheme. This will allow us to distinguish particles from noise more accurately, and will improve the accuracy of the measurement in the axial direction (de Jong & Meng 2007). Finally, by implementing a more precise injection scheme, we will be able to investigate the time dependence of the RDF and compare its transient behaviour to the DNS.

This work was supported by the NASA Microgravity Fluid Physics Program grants NNCO5GA45G and NNCO5GA37G, by the National Science Foundation through grants CTS-0112514 and PHY-0554675 and by the New York State office of Science, Technology and Academic Research (NYSTAR) under contract number 3538479. J.P.L.C.S. acknowledges support from the Brazilian Ministry of Education through the CAPES agency.

REFERENCES

Aliseda, A., Cartellier, A., Hainaux, F. & Lasheras, J. C. 2002 Effect of preferential concentration on the settling velocity of heavy particles in homogeneous isotropic turbulence. *J. Fluid Mech.* **468**, 77–105.

Bec, J., Biferale, L., Cencini, M., Lanotte, A., Musacchio, S. & Toschi, F. 2007 Heavy particle concentration in turbulence at dissipative and inertial scales. *Phys. Rev. Lett.* **98**, 084502.

Benedict, L. H. & Gould, R. D. 1996 Towards better uncertainty estimates for turbulence statistics. *Exps. Fluids* **22**, 129–136.

Berrut, J. P. & Trefethen, L. N. 2004 Barycentric Lagrange interpolation. *SIAM Rev.* **46**, 501–517.

Birouk, M., Chauveau, C., Sarh, B., Quilgars, A. & Gökalp, I. 1996 Turbulence effects on the vaporization of monocomponent single droplets. *Combust. Sci. Technol.* **113–114**, 413–428.

Boivin, M., Simonin, O. & Squires, K. D. 1998 Direct numerical simulation of turbulence modulation by particles in isotropic turbulence. *J. Fluid Mech.* **375**, 235–263.

Brucker, K. A., Isaza, J. C., Vaithianathan, T. & Collins, L. R. 2007 Efficient algorithm for simulating homogeneous turbulent shear flow without remeshing. *J. Comput. Phys.* **225**, 20–32.

Cao, L., Pan, G., Woodward, S. & Meng, H. 2007 Hybrid digital holographic imaging system for 3D dense particle field measurement. In *7th Intl Symp. on Particle Image Velocimetry*. PIV2007.

Chun, J., Koch, D. L., Rani, S., Ahluwalia, A. & Collins, L. R. 2005 Clustering of aerosol particles in isotropic turbulence. *J. Fluid Mech.* **536**, 219–251.

Collins, L. R. & Keswani, A. 2004 Reynolds number scaling of particle clustering in turbulent aerosols. *New J. Phys.* **6**, 119.

Eaton, J. K. & Fessler, J. R. 1994 Preferential concentration of particles by turbulence. *Intl J. Multiphase Flow* **20**, 169–209.

Falkovich, G., Fouxon, A. & Stepanov, M. G. 2002 Acceleration of rain initiation by cloud turbulence. *Nature* **419**, 151–154.

Grassberger, P. & Procaccia, I. 1983 Characterizations of strange attractors. *Phys. Rev. Lett.* **50**, 346–349.

Holtzer, G. L. & Collins, L. R. 2002 Relationship between the intrinsic radial distribution function for an isotropic field of particles and lower-dimensional measurements. *J. Fluid Mech.* **459**, 93–102.

de Jong, J. & Meng, H. 2007 Digital holographic particle validation via complex wave. *Appl. Optics* **46**, 7652–7661.

de Jong, J., Cao, L., Woodward, S., Salazar, J. P. L. C., Collins, L. R. & Meng, H. 2007 Dissipation measurement in zero-mean-flow isotropic turbulence. *Exps. Fluids* (submitted).

Kline, S. J. & McClintock, F. A. 1953 Describing uncertainties in single-sample experiments. *Mech. Engng* **75**, 3–8.

McQuarrie, D. A. 1976 *Statistical Mechanics*. Harper & Row.

Maxey, M. R. 1987 The gravitational settling of aerosol particles in homogeneous turbulence and random flow fields. *J. Fluid Mech.* **174**, 441–465.

Maxey, M. R. & Riley, J. J. 1983 Equation of motion for a small rigid sphere in a nonuniform flow. *Phys. Fluids* **26**, 883–889.

Meng, H., Pan, G. & Pu, Y. 2004 Holographic particle image velocimetry: from film to digital recording. *Measurement Sci. Technol.* **15**, 673–685.

Owen, R., Zozylya, A., Benoit, M. & Klaus, D. 2002 Microgravity materials and life sciences research applications of digital holography. *Appl. Optics* **41**, 3927–3935.

Pan, G. 2003 Digital holographic imaging for 3D particle and flow measurement. PhD thesis, State University of New York at Buffalo.

Pan, G. & Meng, H. 2003 Digital holography of particle fields: reconstruction by use of complex amplitude. *Appl. Optics* **42**, 827–833.

Reade, W. C. & Collins, L. R. 2000*a* Effect of preferential concentration on turbulent collision rates. *Phys. Fluids* **12**, 2530–2540.

Reade, W. C. & Collins, L. R. 2000*b* A numerical study of the particle size distribution of an aerosol undergoing turbulent coagulation. *J. Fluid Mech.* **415**, 45–64.

Saw, E. W., Shaw, R. A., Ayyalasomayajula, S., Chuang, P. Y. & Gylfason, A. 2007 Inertial clustering of particles in high-Reynolds-number turbulence. *Phys. Rev. Lett*. (submitted).

Shaw, R. A. 2003 Particle–turbulence interactions in atmospheric clouds. *Annu. Rev. Fluid Mech.* **35**, 183–227.

Shaw, R. A., Reade, W. C., Collins, L. R. & Verlinde, J. 1998 Preferential concentration of cloud droplets by turbulence: effects on the early evolution of cumulus cloud droplet spectra. *J. Atmos. Sci.* **55**, 1965–1976.

Squires, K. D. & Eaton, J. K. 1991 Preferential concentration of particles by turbulence. *Phys. Fluids* A **3**, 1169–1178.

Sreenivasan, K. R. 1995 On the universality of the Kolmogorov constant. *Phys. Fluids* **7**, 2778–2784.

Sundaram, S. & Collins, L. R. 1997 Collision statistics in an isotropic particle-laden turbulent suspension. Part 1. Direct numerical simulations. *J. Fluid Mech.* **335**, 75–109.

Sundaram, S. & Collins, L. R. 1999 A numerical study of the modulation of isotropic turbulence by suspended particles. *J. Fluid Mech.* **379**, 105–143.

Wang, L.-P. & Maxey, M. R. 1993 Settling velocity and concentration distribution of heavy particles in homogeneous isotropic turbulence. *J. Fluid Mech.* **256**, 27–68.

Wang, L.-P., Wexler, A. S. & Zhou, Y. 2000 Statistical mechanical description and modelling of turbulent collision of inertial particles. *J. Fluid Mech.* **415**, 117–153.

Witkowska, A., Brasseur, J. G. & Juvé, D. 1997 Numerical study of noise from isotropic turbulence. *J. Comput. Acoust.* **5**, 317–336.

Wood, A. M., Hwang, W. & Eaton, J. K. 2005 Preferential concentration of particles in homogeneous and isotropic turbulence. *Intl J. Multiphase Flow* **31**, 1220–1230.

Xu, L., Jericho, M., Meinertzhagen, I. & Kreuzer, H. 2001 Digital in-line holography for biological applications. *Proc. Natl Acad. Sci.* **98**, 11 301–11 305.

Zaichik, L. I. & Alipchenkov, V. M. 2003 Pair dispersion and preferential concentration of particles in isotropic turbulence. *Phys. Fluids* **15**, 1776–1787.